

ARECIBO S-BAND RADAR CHARACTERIZATION OF THE MERCURIAN NORTH POLAR DEPOSITS.

E. G. Rivera-Valentín¹, H. M. Meyer², P. A. Taylor¹, S. S. Bhiravarasu³, M. C. Nolan⁴, N. L. Chabot², and A. K. Virkki⁵. ¹Lunar and Planetary Institute, USRA, ²Johns Hopkins University Applied Physics Laboratory, ³Space Applications Centre, ISRO, ⁴Lunar and Planetary Laboratory, Univ. of Arizona, ⁵Arecibo Observatory, UCF.

Introduction: After determining Mercury's correct rotation rate [1], the next notable ground-based, radar-enabled discovery at Mercury was the identification of radar-bright features at its poles [2,3], which scattering models suggested were due to the presence of water ice [4]. Indeed, the MESSENGER spacecraft confirmed that radar-bright features are typically associated with permanently shadowed regions (PSRs) [5,6] that are on average hydrogen-rich [7]. Local cratering and topography indicate the ice deposits are some few meters thick [8] and were emplaced within the last 300 Ma [9]. Some of the ice was found to be semi-continuous surficial deposits within large polar craters [10]; however, MESSENGER's Mercury Laser Altimeter (MLA) also found that some radar-bright deposits in PSRs were darker in MLA than the surrounding terrain, indicating ice burial beneath a low-reflectance, perhaps organic-rich, material [11]. Such local-scale variations in, e.g., burial depth and spatial coverage, would manifest as differences in radar backscatter.

The wealth of geological and compositional information provided by the MESSENGER mission now provides excellent context to better decipher radar data products. Here we report on analysis of our recent Mercury radar observations using the Arecibo Observatory in Puerto Rico, the first since the end of the MESSENGER mission. We used machine learning algorithms to identify small-scale variations in radar backscatter in order to constrain the characteristics of Mercury's north polar ice deposits.

Observations: We conducted monostatic observations of Mercury using the Arecibo S-band (12.6 cm; 2380 MHz) planetary radar system during the inferior conjunctions in July 2019 and June 2020. During conjunction, Mercury was at a round-trip light time of some 9 minutes. The subradar latitude during these campaigns allowed for observations of only the north pole. We used the long-code delay-Doppler radar imaging method [12] with a baud of 10 μ s at 2 samples per baud resulting in, at best, 750 m/pixel resolution in the delay dimension. Echoes in both the opposite circular (OC) and same circular (SC) polarization as transmitted were recorded. In 2019, an issue with the low-noise amplifiers at Arecibo resulted in poor quality OC data. The issue was not remedied in time for our 2020 observing runs; however, the poor channel had been switched to SC. Thus, SC data is from the 2019 campaign and OC data is from the 2020 campaign.

Radar Analysis: For every delay-Doppler radar image, Mercury's projected size and rotation were used to calculate the expected Doppler values at every delay bin. This let us reduce the radar images to include only backscatter from Mercury. Using the subradar latitude and longitude for every transmit-receive cycle, the corresponding heliocentric position was calculated for every pixel from its delay-Doppler coordinates, then projected onto a polar stereographic map (e.g., [13,14]). Each map was verified by georeferencing with prominent features using MESSENGER's Mercury Dual Imaging System (MDIS) data. The final radar-backscatter maps are sums of the campaign and were z-score normalized (i.e., such that the average of the pixel values in the image is zero with a standard deviation of one). As an example, in Fig. 1 we show the SC radar backscatter image in polar stereographic projection resulting from our six-day observing campaign in 2019. The radar-bright features agree well with PSR locations, including the most striking deposits on the floors of Prokofiev, Kandinsky, Tolkien, Chesterton, and Tryggvadóttir with abundant smaller deposits also evident.

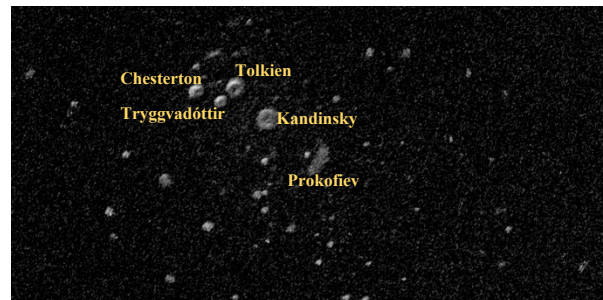


Figure 1: Z-score normalized SC radar-backscatter image of Mercury's north pole. Only z-score values greater than zero are shown. Major feature names are overlain on the image.

k-means clustering: Comparing variations in radar backscatter is not robust pixel by pixel as the true uncertainty of each pixel value is not well constrained. Here, in order to confidently identify small-scale variations in the radar characteristics of the polar region, we used *k-means* clustering, which is a machine learning algorithm that partitions data into groups by minimizing within-cluster variances. Typically, *k-means* requires the user to predefine the number of clusters; however, the technique can be made unsupervised by way of the CH index [15], which identifies the best number of groups by maximizing the ratio of the sum of between-cluster dispersion and of inter-cluster dispersion. Radar-

backscatter values were then represented by their cluster mean and standard deviation allowing for robust comparison between pixels. For confidence, only the top two clusters representing the highest radar return were analyzed; signals that were clustered into lower classes were considered indistinguishable from noise. This choice was verified for a random selection of images by comparing the final cluster maps to previous radar images of Mercury [16] and MDIS data.

To verify that the clustering is physically realistic, we show in Fig. 2 a zoomed in SC radar-backscatter cluster map of Prokofiev (112 km; 86°N, 296.3°W) and Kandinsky (60 km; 87.9°N 78.8°W) craters overlain on an MDIS image identifying areas that are permanently in shadow. Cluster locations correspond well with PSR locations. Furthermore, areas at the boundary of shadowed regions, including discontinuous areas within large PSRs (e.g., within Prokofiev), are associated with either the lower class (cyan) or are clustered below the noise. These regions would, thus, be expected to either have deeper ice deposits or less ice. Another example is the PSR within Kandinsky crater, which has a long discontinuity near the center. Our clustering shows that this area is not associated with significant radar backscatter. This visual inspection provides confidence that the technique leads to meaningful results.

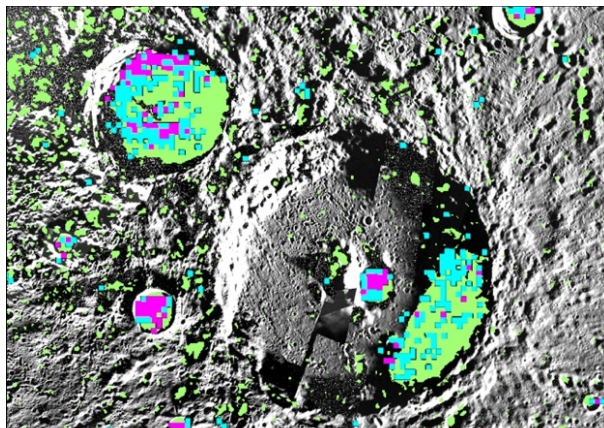


Figure 2: MESSENGER MDIS mosaic of Mercury's north pole overlain with a *k*-means cluster map (2 km/pxl) of SC radar backscatter from the 2019 campaign. Magenta is the highest class followed by cyan. Green denotes PSRs.

Discussion: In Fig. 3, we show the Mercurian north polar terrain as a *k*-means cluster map of the SC radar backscatter summed over the six-day observing campaign. To improve signal analysis, the resolution of the base radar map used for clustering was reduced to some 2 km/pixel. Because the polar deposits are brightest in SC, we only analyzed the data from the 2019 campaign.

In Fig. 3, significant local scale variations in the radar-scattering properties of the north polar deposits are distinguishable in both the large and small craters.

The spatial variation of these clusters indicates that there may exist differences in the radar-scattering properties of these deposits. These differences may result from variations in ice abundance or burial depth. Additionally, heterogeneities in the deposits are discernible. For example, Tolkien, Chesterton, and Tryggvadóttir have large areas that cluster into the highest radar-backscatter class (magenta) while Prokofiev and Kandinsky have relatively smaller similar areas and are dominated by the lower radar-backscatter class (cyan). This may indicate that the largest continuous ice deposits may be likely found within Tolkien, Chesterton, and Tryggvadóttir rather than Prokofiev or Kandinsky.

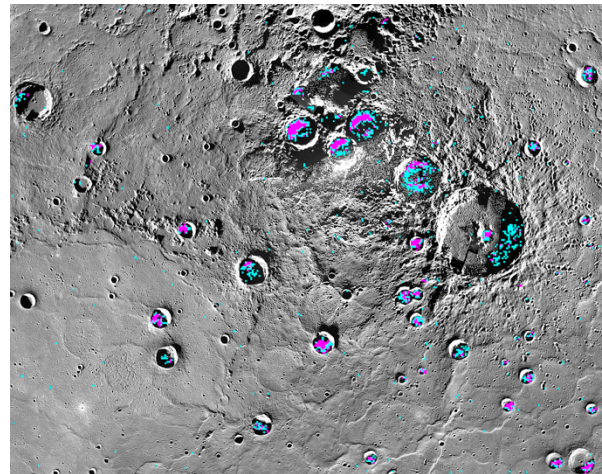


Figure 3: MESSENGER MDIS mosaic of Mercury's north pole overlain with a *k*-means cluster map of SC radar backscatter summed over our six-day campaign in 2019 with magenta being the highest class followed by cyan.

References: [1] Pettengill, G. H. & Dyce, R. B. (1965) *Nature* 206, 1240. [2] Slade, M. A. et al. (1992) *Science* 258, 635-640. [3] Harmon, J. K. & Slade, M. A. (1992) *Science*, 258, 640-643. [4] Butler, B.J. et al. (1993) *JGR* 98, 15003-15021. [5] Chabot, N. L. et al. (2012) *GRL* 39, L09204. [6] Deutsch, A. N. et al (2016) *Icarus* 280, 158-171. [7] Lawrence, D. J. et al. (2013) *Science* 339, 292-296. [8] Susorney, H. C. M. et al. (2019) *Icarus* 323, 4045. [9] Deutsch, A. N. et al. (2019) *EPSL* 520, 26-33. [10] Chabot, N. L. et al. (2014) *Geology* 42, 1051-1054. [11] Neumann, G. A. (2013) *Science* 339, 296-300. [12] Harmon, J. K. (2002) *IEEE Trans. G&RS* 40, 1904-1916. [13] Pettengill, G. H. et al. (1974) *The Moon*, 10, 3-16. [14] Campbell, B. A. (2002) Cambridge Univ. Press. [15] Calinski, T. & Harabasz, J. (1974) *Comm. in Stats.* 2, 1-27. [16] Harmon, J. K. et al. (2011) *Icarus* 211, 37-50.

Acknowledgements: This research was supported by NASA through NEOO under Grant Nos. NNX13AQ46G and 80NSSC19K0523, and DDAP under Grant No. 80NSSC19K0881. The Arecibo Observatory is a facility of the National Science Foundation with the Arecibo Planetary Radar Project fully funded by NASA.